High-Fidelity CFD Methods for the Simulation of Propeller Stall Flutter*

Ross J. Higgins[†], Antonio Jimenez-Garcia[‡] and George N. Barakos[§]
University of Glasgow, James Watt South Building, Glasgow, G12 8QQ, U.K.

Nicholas Bown[¶]
Dowty Propellers, Anson Business Park, Cheltenham Road East, Gloucester, GL2 9QN, U.K.

A time-marching aeroelastic method developed for the study of propeller flutter is presented and validated. Propeller flutter can take many forms with stall, whirl and classical flutter being the primary responses. These types of flutter require accurate capture of the non-linear aerodynamics associated with propeller blades. Stall flutter in particular needs detailed unsteady flow modelling. With the development of modern propeller designs potentially adjusting the flutter boundary and the development of faster computing power, CFD is required to ensure accurate capture of aerodynamics. Given the lack of reliable experimental stall flutter data for propellers, the method was focused on observing the correct qualitative behaviour with a comparison made between *URANS* and Scale-Adaptive Simulation (*SAS*).

Nomenclature

Latin

c	=	Blade chord (m)
f_m^s	=	Modal force on solid s for the m-th mode (N/m.kg)
n_m^s	=	Number of modes for solid s (-)
p	=	Pressure (Pa)
$\mathbf{p}(p,t)$	=	Pressure vector at a point p, and at a time t (N/m^2)
$\mathbf{P}$	=	Position of node p (m)
R	=	Blade Radius (m)
$\mathbf{R_{i,j,k}}$	=	Vector of flux residual for the the cell i, j, k
R/c	=	Blade Aspect Ratio (-)
Re	=	Reynolds number based on the rotor blade chord and tip-speed

*An early version was presented at the 2019 AIAA SciTech Forum, San Diego, California, USA, January 7-11, 2019.
[†]PhD Student, CFD Laboratory.
[‡]Post-Doctoral Researcher, CFD Laboratory.
[§]Professor, CFD Laboratory, corresponding author.
[¶]Project Engineer, Dowty Propellers.

t = Time (s)

$V_{i,j,k}$ = Volume of the cell i, j, k

$\mathbf{W}_{i,j,k}$ = Vector of conservative variables for the cell i, j, k

$w_i(x)$ = Interpolation weight (-)

Greek

α_m^s = Model amplitude of mode m of solid s (m/kg)

ζ_m = Damping coefficient (-)

ρ = Fluid density (kg/m^3)

ψ_m^s = Normalised m^{th} mode displacement of solid s (m/kg)

ψ^s = Normalised displacement of solid s (m/kg)

ω_m = Natural frequency of mode m

Ω_{CV} = Control volume size

Subscripts

i, j, k = Mesh cell indices

Introduction

Propeller flutter manifests in a variety of different ways. This includes classic, stall and whirl flutter. These types of flutter, particularly whirl and stall, require detailed modelling of the aerodynamics and structural response of a propeller. For stall flutter, the non-linear aerodynamics is a result of the detached flow-field which triggers the aeroelastic excitation.

Successful capture of such aerodynamic interactions allows for increased accuracy in surface loads, and increased accuracy in predicting the resultant flutter boundary. From this base, and with the development of faster computing power, a time-marching aeroelastic method has been developed which couples Computational Fluid Dynamics (CFD) and Computational Structural Dynamics (CSD). Flutter of any type is a result of a fluid-structure interaction and the method was derived based on this assumption.

Propeller stall flutter research began with the analysis of the Spitfire blade by Sterne in 1945 [1]. Static experiments were conducted to determine the flutter boundary of the propeller, with the boundary presented in the form of the blade pitch versus blade rotational velocity. The experiment found that the blade would flutter at a much lower velocity within a specific pitch region. This reduction in the flutter boundary corresponded to the presence of stall. The Spitfire blade used during this investigation was made of compressed wood and, as a result, there is the potential for the structural

properties to vary during the manufacturing process, with a strong impact on the flutter boundary.

In 1955, [2] Baker conducted a static experimental investigation into the effects of various parameters on the flutter boundary of an untwisted model propeller blade. These parameters included the effects of the blade structure, the blade geometry, and the freestream flow conditions. Baker concluded that the positioning of the section centre-of-gravity, introduction of sweep, increase in section thickness and Mach number all had a significant effect on the flutter boundary. To ensure satisfactory aerodynamic performance, thin aerofoil sections are required at high speed, therefore, any change in section thickness would decrease performance. Baker did note that the resultant flutter boundaries were not within the normal operating cruise conditions for typical propellers, and it was only during take-off *like* conditions that the blades were found to suffer from stall flutter. The stall flutter boundary is also presented in non-dimensional form, with no other measured parameters presented.

In 1956, Hubbard *et al.* followed on from the work conducted by Baker [3]. The primary aim was to determine the effect of Mach number and structural damping on the flutter boundary. During the experiment, strain gauges were used to measure the vibratory stress levels with runs conducted at a fixed pitch angle, only varying the rotational velocity. The combined works of Baker and Hubbard *et al.* allowed for a detailed understanding of propeller stall flutter due to the volume of parameters investigated. However, the blades used in these experiments do not represent a realistic modern blade and this has a significant effect on the observed flutter boundary.

A similar investigation was conducted by DOWTY Propellers in 1979 [4]. The aim was to determine the torsional stress levels, and hence the flutter characteristics, of the Commander propeller blade when spun at fixed pitch over a range of rotational velocities. The torsional stress levels were measured via strain gauges placed along the propeller radius. During the first stage of the test, high levels of torsional stress were seen for a given pitch angle, with the test terminated due to excessive oscillations. Upon examination of the propeller apparatus, the propeller crosshead had failed and hence a redesign of the crosshead was required. Following this, overspeed and 30 minute power run tests were completed at lower blade pitch angles, without further attempts to probe the stall flutter boundary. From the torsional stress results, a clear stall flutter boundary was observed with a sharp increase in stress seen around 1650 rpm.

In 1985, Smith conducted a static experimental investigation into three prop-fan model propellers [5]. These models were designated SR-2, SR-3 and SR-5, with the blades featuring increasing levels of sweep from the unswept, SR-2, to the highly swept, SR-5. In a similar manner to the DOWTY tests, for a fixed pitch angle, the propeller rotational velocity was increased to maximum before returning to its baseline value. Vibratory stress levels were measured via strain gauges. A comparison was made to the work conducted in the NASA/Lewis wind tunnel facilities. In terms of amplitude and trend, close agreement was found between the two investigations. Smith also conducted a numerical analysis on the propeller blades. The stability analysis was developed primarily for classical flutter using a linear eigenvalue approach, with a modal analysis module also available. The method was extended to include unsteady aerodynamic effects via two-dimensional aerofoil sections. Smith found stall flutter to occur on both the SR-2 and

SR-3 propeller blades, with stall flutter only occurring in the SR-5 blade at very high rotational velocities. It is noted that the experimental results were limited to a maximum stress level, therefore the full boundary of these propellers may not be known. The torsional stress response was also found to be linear, therefore a clear boundary cannot be observed from the stress data.

Reddy and Kaza in 1989 conducted a numerical investigation into the SR-2 propeller [6]. They utilised the Gormont dynamic stall model [7] to capture the non-linear aerodynamics. The numerical results were seen to predict the same trends as the experiments, however, the exact values are conservative.

In 2007, Delamore-Sutcliffe conducted a numerical investigation into propeller stall flutter [8]. It involved the derivation of a non-linear aerodynamic model which focused on stalled cross sections. The aerodynamic model was validated via two-dimensional experimental results, and was coupled with the Brooks and Houbolt equations of motion for a rotating beam. Comparisons were made to the experimental results of Baker [2] with close correlation found between the results at low pitch angles.

Ognev in 2011 investigated different unsteady aerodynamic models and their influence on the determined flutter boundary [9]. He used Theodorsen's model, two cascade based models and a three-dimensional model. These models were coupled with linearised equations of motion and were compared to the experimental work of Hubbard *et al.* [3]. A fair agreement between the experimental and numerical results were found.

In addition to these full propeller stall flutter investigations, many studies have been conducted in recent times which focused on two-dimensional aerofoils. Such investigations made use of pitch and plunge rigid models [10–12], cyber-physical models (where the structural response of the aerofoil is given based upon a known set of derived equations of motion) [13, 14], or if numerical, utilised dynamic stall based aerodynamic models [15, 16]. The use of such studies can only provide fundamental analysis into aerofoil stall response, with conservative boundaries when applied to true test cases.

As observed from literature, very few experimental investigations have been conducted, with a limited number of measured parameters presented. For each experimental investigation, the structural properties are unknown, resulting in an estimation of these properties. A summary of the pros and cons associated with each experimental test case is presented below in Table 1. In terms of numerical studies, all have focused on the inclusion of non-linear aerodynamics through unsteady dynamic stall models applied to two-dimensional sections. A summary can be found in Table 2.

Due to the limitations in the number of measured parameters and test cases, this paper will focus on observing the correct qualitative behaviour of propeller stall flutter. Literature has found lower fidelity models to perform reasonably at low pitch angles, however, the calculated boundaries are seen to be conservative when significant detached flow is present. To improve design and expand the operating conditions for propellers, capturing of three-dimensional stall effects is vital in the accurate estimation of the flutter boundary.

Test Case	Pros	Cons	Conditions
Spitfire Propeller [1]	*1:* Stall flutter boundary given *2:* Known geometry	*1:* Wooden blade *2:* Structural properties	*rpm:* 800 – 1800 *Pitch:* 8° – 32°
Baker/Hubbard Models [2, 3]	*1:* Dimensionless boundary *2:* Extensively analysed	*1:* Structural properties *2:* Non-realistic blades (model only)	*Pitch:* 5° – 35°
Commander Propeller [4]	*1:* Torsional stress boundary *2:* Known geometry *3:* Realistic blade (in-service) *4:* Trusted by manufacturers	*1:* Structural properties estimated	*rpm:* 1400 – 1800 *Pitch:* 26° – 28°
SR Blades [5]	*1:* Damping & stress boundaries *2:* Range of blade configurations *3:* Extensively analysed	*1:* Structural properties *2:* Full boundary not known	*rpm:* 2000 – 10000 *Pitch:* 20° – 50° *Scale:* $^1/_8$

Table 1 Summary of experimental test cases.

Test Case	Summary	Conditions	Date
Reddy and Kaza [6] *SR-2 Propeller*	2D aerofoil sections Dynamic stall model Modal analysis Conservative results	*rpm:* 2000, 5000, 8500 *Pitch:* 30° , 50°	1989
Delamore-Sutcliffe [8] *Baker/Hubbard Models*	2D aerofoil sections Validated via 2D experiments Coupled with rotating beam equations of motion Eigenvalue analysis Deviations from experiment at high pitch angles	*Pitch:* 0° – 20°	2007
Ognev [9] *Baker/Hubbard Models*	2D aerofoil sections Aerodynamics supplied by various unsteady models Eigenvalue analysis Fair agreement to experiments	*rpm:* 500 – 2500 *Pitch:* −20° – 10°	2011

Table 2 Summary of numerical test cases.

Computational Methodology: HMB3

For this investigation, a time-marching aeroelastic method has been developed. It uses the in-house flow solver HMB3, and couples Computational Fluid Dynamic (CFD) and Computational Structural Dynamics (CSD). The core functionality of HMB3 is CFD, however its use has been extended in recent years to include whole engineering applications, including helicopter rotor aeroelasticity[17], propeller aeroacoustics[18], flight mechanics[19] and missile trajectory prediction[20].

Computational Fluid Dynamics

Previous investigations using HMB3 have provided propeller flow validation in both installed and isolated conditions, by comparison with the experimental results of the JORP propeller [21] and the IMPACTA wind tunnel tests [22, 23]. Good agreement was found in terms of aerodynamics and acoustics [18, 24]. HMB3 solves the Navier-Stokes equations in integral form and are discretised using a cell-centred finite volume approach on a multi-block grid. The spatial discretisation of these equations leads to a set of ordinary differential equations in time,

$$\frac{d}{dt}(\mathbf{W}_{i,j,k}V_{i,j,k}) = -\mathbf{R}_{i,j,k}(\mathbf{w}) \tag{1}$$

where i, j, k represent the cell index, $\mathbf{W}$ and $\mathbf{R}$ are the vector of conservative variables and flux residual respectively and $V_{i,j,k}$ is the volume of the cell i, j, k. Greater detail on the numerical techniques employed can be found within the previous investigations conducted using HMB3 [17–20, 24–27]. Several turbulence models, of both URANS and hybrid LES/URANS families, are available in the HMB3 solver. For this investigation the standard $k-\omega$ turbulence model will be compared to the hybrid LES/URANS method known as Scale Adaptive Simulation (SAS) [28, 29]. The *SAS* formulation allows for the dynamic adjustment of the von Karman length scale to produce an *LES-like* solution. HMB3 *SAS* simulations have been conducted in the past focusing on transonic cavity flows [30] and missile projection [31]. Because this investigation requires the deformation and relative motion of the propeller blade, in order to achieve this, the chimera method is used[32]. ICEM-Hexa™ of ANSYS is used to generate all structured grids for this investigation.

Computational Structural Dynamics

The aeroelastic framework of HMB3 is based on the modal method [20]. This method uses externally computed structural modes and a mesh deformation module based on the inverse distance weighting interpolation. The modal approach was selected in order to reduce computational cost as it expresses solid deformations as functions of the structure's eigenmodes.

A NASTRAN finite element model is created in order to obtain the structural mode shapes and frequencies. The finite element model uses non-linear PBEAM elements to model the structure's mass and inertia distribution along the span, with rigid bars (RBAR) elements used to connect the PBEAM node to each of the fluid mesh points at the given section. A non-linear static analysis (SOL 106) is computed to obtain the mode shapes and frequencies, along with a static deformation to rigid loads.

At the beginning of each computation, the structural modes are interpolated from the CSD to the CFD grid. The interpolation is performed with the Moving Least Square method (MLS). The MLS method allows for sufficient accuracy in terms of the modal force and displacement estimations due to the fact these values are calculated based

upon the CFD grid without further interpolation to the CSD.

Computation of Modal Loads and Amplitudes

The CFD computation is performed on the deformed mesh to obtain the solution at $t + \Delta t$. The pressure is then summed over the undeformed mesh points to compute the modal loads $f_m^s(t)$ on the solid (s) for the m-th mode at time t:

$$f_m^s(t) = \sum_{p=1}^{n_s} \mathbf{p}(p,t).\phi_m^s(p) \tag{2}$$

with n_s the number of CFD points on the solid s, $\mathbf{p}(p,t)$ the pressure at a point p in N/m^2, and $\phi_m^s(p)$ the mode displacement at the point p for the m-th mode of the solid s normalised by the generalised mass set to 1kg. The modal load unit is $N/m.kg$.

The shape of the solid s, $\phi^s(t)$, is described as a sum of eigenvectors ϕ_m^s :

$$\phi^s(t) = \phi_0^s + \sum_{m=1}^{n_m^s} \alpha_m^s(t)\phi_m^s \tag{3}$$

with n_m^s the number of modes on the solid s, and ϕ_0^s the undeformed shape. The problem is then reduced to solving for the coefficient α_m^s. In the modal approach, the coefficient can be obtained by solving the following differential equation:

$$\frac{\partial^2 \alpha_m^s}{\partial t^2} + 2\zeta_m \omega_m \frac{\partial \alpha_m^s}{\partial t} + \omega_m^2 \alpha_m^s = f_m^s(t) \tag{4}$$

For stability purposes, the analysis starts with a strong damping coefficient of $\zeta_m = 0.1$ for each mode. This high structural damping is used to control the oscillations created during the initial steps of the simulation, due to the sudden change in the forces applied to a second order system. Once the solid reaches an acceptable level of deformation, the damping is then gradually brought to its final value of $\zeta_m = 0.01$.

The modal method differential equation (Equation 4) is then explicitly solved using the leap-frog method. To ensure stability of higher modal frequencies, each time-step is solved in N_i inner time-steps of size $\Delta t_i = \Delta t / N_i$. The modal force at the time $t_i = t + i\Delta t_i$ is :

$$f_m^s(t_i) = f_m^s(t) + \frac{i(f_m^s(t + \Delta t) - f_m^s(t))}{N_i} \tag{5}$$

The m-th amplitude α_m^s is then assessed for inner time-step $t_i + 1$:

$$[\alpha_m^s]_{t_i+1} = [\alpha_m^s]_{t_i} + \left[\frac{\partial \alpha_m^s}{\partial t_i}\right]_{t_i} \Delta t_i + \frac{1}{2}\left[\frac{\partial^2 \alpha_m^s}{\partial t_i^2}\right]_{t_i} \Delta t_i^2 \tag{6}$$

The time derivatives of the modal amplitudes is computed as:

$$\begin{aligned}\left[\frac{\partial^2 \alpha_m^s}{\partial t_i^2}\right]_{t_i+1} &= [f_m^s]_{t_i} - \omega_m^2 [\alpha_m^s]_{t_i} - 2\zeta\omega_m \left[\frac{\partial \alpha_m^s}{\partial t_i}\right]_{t_i} \\ \left[\frac{\partial \alpha_m^s}{\partial t_i}\right]_{t_i+1} &= \left[\frac{\partial \alpha_m^s}{\partial t_i}\right]_{t_i} + \frac{1}{2}\left(\left[\frac{\partial^2 \alpha_m^s}{\partial t_i^2}\right]_{t_i} + \left[\frac{\partial^2 \alpha_m^s}{\partial t_i^2}\right]_{t_i+1}\right)\Delta t_i\end{aligned} \tag{7}$$

A flow chart showing the different stages of the method is shown in Figure 1

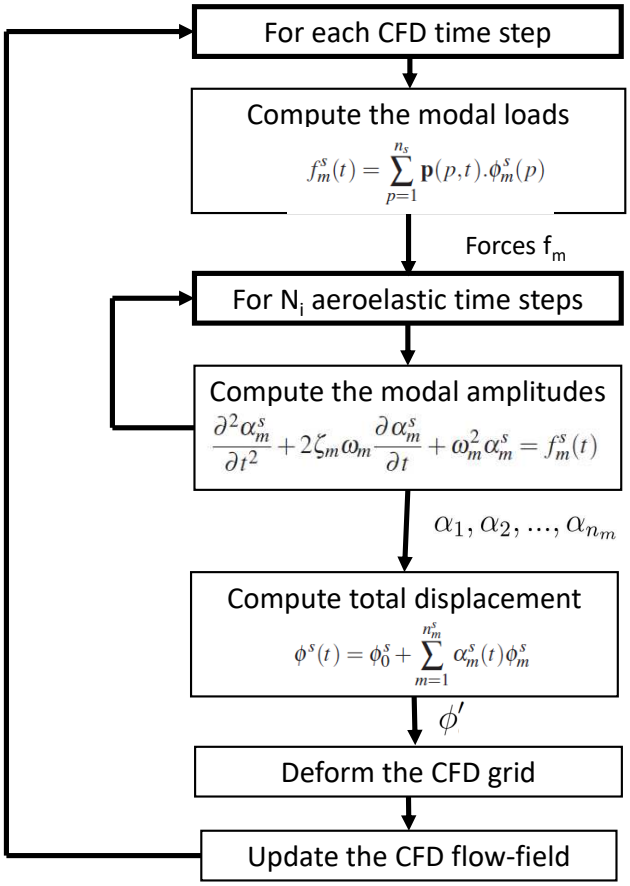

Fig. 1 Illustration of the computational structural dynamics strategy during each CFD time-step.

Deformation of the Volume Mesh

To adapt the volume mesh to the surface of the deformed solid, a mesh deformation algorithm has been implemented in HMB3 based on Inverse Distance Weighting (IDW) [33]. IDW interpolates the values at given points with a weighted average of the values available at a set of known points. The weight assigned to the value at a known point is proportional

to the inverse of the distance between the known and the given point. Biava *et al.* [34] used this method to optimise rotor blade shapes in HMB3, with no reduction in mesh quality found.

Given N samples $\mathbf{u}_i = u(\mathbf{x}_i)$ for $i = 1, 2, ..., N$, the interpolated value of the function $\mathbf{u}$ at a point $\mathbf{x}$ using IDW is given by:

$$\mathbf{u}(\mathbf{x}) = \begin{cases} \dfrac{\sum_{i=1}^{N} w_i(\mathbf{x})\mathbf{u_i}}{\sum_{i=1}^{N} w_i(\mathbf{x})}, & \text{if } d(\mathbf{x}, \mathbf{x_i}) \neq \mathbf{0} \text{ for all } \mathbf{i} \\ \mathbf{u_i}, & \text{if } d(\mathbf{x}, \mathbf{x_i}) = \mathbf{0} \text{ for some } \mathbf{i} \end{cases} \tag{8}$$

where

$$w_i(\mathbf{x}) = \frac{\mathbf{1}}{\mathbf{d}(\mathbf{x}, \mathbf{x_i})^{\mathbf{p}}} \tag{9}$$

In the above equations, p is any positive real number (called the *power parameter*) and $d((\mathbf{x}), (\mathbf{y}))$ is the Euclidean distance between $(\mathbf{x})$ and $(\mathbf{y})$.

The method in its original form becomes expensive as sample data sets get larger. An alternative formulation of the Shepard's method, which is better suited for large-scale problems, has been proposed by Renka [35] where the interpolated value is calculated using only the k nearest neighbours within an R-sphere (k and R are given, fixed, parameters) shown in green in Figure 2. The weights are slightly modified in this case:

$$w_i(\mathbf{x}) = \left(\frac{\max(\mathbf{0}, \mathbf{R} - \mathbf{d}(\mathbf{x}, \mathbf{x_i}))}{\mathbf{R}\mathbf{d}(\mathbf{x}, \mathbf{x_i})} \right)^{\mathbf{2}}, \quad \mathbf{i} = \mathbf{1}, \mathbf{2}, ..., \mathbf{k}. \tag{10}$$

If this interpolation formula is combined with a fast spatial search structure for finding the k nearest points, it yields an efficient interpolation method suitable for large-scale problems [33].

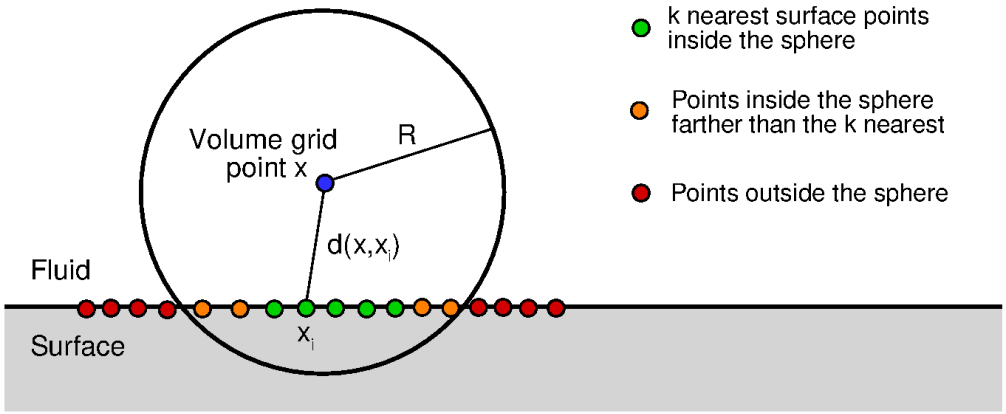

Fig. 2 Illustration of the point selection process in order to compute the IDW weights.

The modified IDW interpolation formula is used in HMB3 to implement mesh deformation in an efficient and robust way to ensure the fast deformation of a large grids without loss of quality. The known displacements of points belonging to solid surfaces represent the sample data, while the displacements at all other points of the volume grid are computed using equation (8) with the weights of equation(10). For fast spatial search of the sample points, an Alternating Digital Tree (ADT) data structure [36] is used. A blending function is also applied to the interpolated displacements, so that they smoothly tend to zero as the distance from the deforming surface approaches R.

Stall Flutter Cases

For this investigation, the Commander propeller blade of DOWTY Propellers was selected. This test case was chosen due to the availability of the experiment data and its application in the Jetprop variants of the Commander aircraft resulting in the blade being applicable in a true engineering environment. The Commander propeller blade was designed by DOWTY Propellers in the 1970's.

Moreover, a rigid dynamic stall investigation was conducted on the 90% R aerofoil section in order to determine the amount of aerodynamic damping associated with that section. As shown in literature [37], the analysis of the pitching aerofoil in dynamic stall can give an indication of stall flutter for that section. From that basis, the NACA 0012 aerofoil section was used for validation, and was selected due to the high amount of experiment data available at different pitching conditions.

Dynamic Stall Investigation

NACA 0012 computational setup

The topology utilised a standard C-grid around the aerofoil with the downstream blocks rotated to coincide with the mean angle of attack. The far-field boundaries were selected to be 15 chord-lengths from the aerofoil section, in all directions. In terms of the mesh, 650 cells were distributed around the aerofoil with 85 cells distributed via an exponential law, clustering to $1 \times 10^{-6}\ C_{ref}$, outward of the aerofoil surface.

Standard two-dimensional boundary conditions were applied to the spanwise boundary faces for an initial verification of the mesh quality and CFD setup, with a spanwise length of 1 chord. This process involved the study of grid size, time-step and number of psuedo-steps per unsteady iteration. The baseline setup for the 2D study is presented in Table 3, with this setup resulting in a converged response.

Following this, the two-dimensional conditions were replaced with periodic boundary conditions. This allows for a quasi-3D simulation where scale-resolving turbulence simulation methods can be implemented. For this investigation standard *URANS* closed with the $k-\omega$ SST turbulence model was compared to SST-*SAS* . For the quasi-3D simulations, the spanwise length was reduced to a quarter chord.

The test conditions for this calculation are presented in Table 3 and correspond to experiments by McAlister in

1982 [38]. These test conditions were selected as they represent typical flow conditions found during the dynamic stall of a helicopter rotor in forward flight.

Commander aerofoil computational setup

In a similar manner to the NACA 0012 investigation, a matched grid was derived for the Commander 90% R section with similar topology, number of grid points and points distribution used. Modifications to the NACA 0012 topology was required in order to account for the blunt trailing edge on the Commander section.

As per the NACA 0012 test case, the same computational setup, in terms of time-step, pseudo steps, CFL and turbulence modelling, was selected. Both standard 2D and quasi-3D simulations were conducted. The selected test conditions for the Commander section is presented in Table 3. These test conditions were selected based upon the Mach number and pitch angle seen within the 3D blade, with a harmonic pitch angle of 5° selected to determine its response. All *SAS* simulation results were phased averaged over 4 revolutions before comparing to standard *URANS* .

Table 3 Dynamic Stall Test Conditions

Parameter	*NACA 0012*	*Commander* 90% *R*
Reynolds Number	2.42×10^6	2.0×10^6
Mach Number	0.184	0.57
Reduced Frequency	0.149	0.12
Pitching Motion	$15° \pm 10° \sin(\omega t)$	$8° \pm 5° \sin(\omega t)$
Steps per Revolution	1600	
Pseudo-Steps per CFD Time-step	200	
Modelling	*URANS* $k-\omega$ SST & *SAS*	

2D Aerodynamic Damping Calculation

To fully determine the stability of the aerofoil section, the amount of aerodynamic damping within the system can be determined via the integration of the pitching moment coefficient with respect to the pitching angle. Such a method was described by Corke in 2015 [37] with the derivation of the aerodynamic damping shown in Equation 11, where C_m^D and C_m^U are the pitching moment coefficients on the downstroke and upstroke, respectively, and α_h being the harmonic pitching angle.

$$\theta_{cycle} = \frac{1}{\pi \alpha_h^2} \int \left(C_m^D - C_m^U \right) \partial \alpha \tag{11}$$

Full 3D Investigation: Commander Propeller Blade

Using the derived time-marching method, the Commander blade was modelled in isolation. During model implementation, simulations were conducted utilising the full propeller, nacelle, wing combination. However, due to the large computational cost associated with such a simulation, and due to the fact that it is the detached flow associated with the reference blade that triggers the aeroelastic excitation (the excitation is then propagated to the additional blades via the nacelle connection with a phase difference seen within the excitation between blades), periodicity in space was assumed. This allows for the reduction of the computational domain to one propeller blade.

The structural model for the Commander blades are based upon the assumption of a solid material blade. The linear mass distribution was calculated as a function of the cross-section area, with the blade inertia based upon the variation in cross-section area.

The baseline propeller design consisted of three blades, with an aspect ratio of ~ 11.0 and chord of $\sim 0.13\ m$.

Computational Setup

Based upon the blade geometry a computation domain of 120° was created with a radial distance from the origin of 5 R/c. The inflow was selected to be also 5 R/c with the outflow 8 R/c from the origin in the vertical direction. A solid cylindrical hub was created from the inflow to outflow.

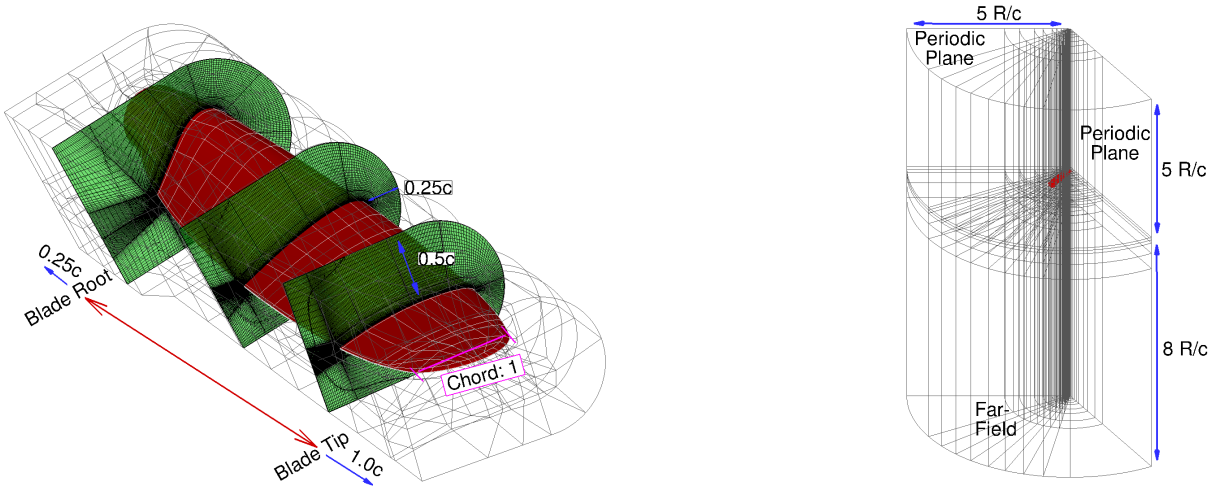

(a) Foreground Grid

(b) Background Grid

Fig. 3 Commander Propeller Computational Domain and Chimera Grid.

The chimera technique was used for the aeroelastic computations and was selected to allow for the deflection of only the blade grid. An O-grid was used for the foreground mesh and this was due to the blunt trailing edge and blade tip design. This was accompanied by a conventional cylindrical background mesh. Presented in Table 4 is the grid sizes used for the mesh convergence study. Similar levels of mean thrust and load oscillations were seen between the three grids from *URANS* rigid simulations, therefore the baseline grid was selected for this study.

Grid level	Coarse	Baseline	Fine
Total Grid Size (*volume cells*)	1, 597, 508	12, 780, 064	18, 857, 888
Foreground	441, 508	3, 532, 064	9, 609, 888
Background	1, 156, 000	9, 248, 000	9, 248, 000

Table 4 Grid convergence study.

A time-step comparison was conducted using 1° , 0.5° and 0.25° steps per propeller revolution, with the change in pressure and viscous vertical load presented in Table 5. The average vertical load for the pressure component is seen to be within 2% for the 0.5° and 0.25° simulations to the baseline time-step. The average amplitude variation of the vertical pressure load is found to be less than 8% for all simulations, with instantaneous maximum values of similar levels seen. The viscous load is seen to be less than 0.05% of the pressure component for all simulations, therefore the change in average and average amplitude is scaled by the pressure component. Very little change in seen between the average viscous loads with all simulations showing similar amplitude levels. In addition to this, three clear frequency peaks were observed between all simulations, thus ensuring that all simulations are able to capture the same content. Due to the match of vertical load levels and captured frequencies, the $1^\circ\ /step$ simulation will be used for this study as this balances the computational cost to level of resolved content.

	Pressure			Viscous		
Time-step	*Average*	Δ *Average (%)*	Δ *Amplitude (%)*	*Average*	Δ *Average (%)**	Δ *Amplitude (%)**
$1^\circ\ /step$	5.832	-	4.28	-2.75×10^{-3}	-	0.013
$0.5^\circ\ /step$	5.932	1.71	7.34	-2.27×10^{-3}	0.007	0.012
$0.25^\circ\ /step$	5.854	0.38	6.53	-2.47×10^{-3}	0.004	0.012

*Scaled by pressure component

Table 5 Average and change in non-dimensional vertical load for the time-step study.

The baseline test conditions for this propeller were based upon the initial starting conditions of the static wind tunnel test [4]. Sea-level conditions were assumed, with the reference velocity and length selected as the tip Mach number at 1400 (rpm) and tip chord length, respectively. Following the convergence of the rigid flow-field at 1400 (rpm), the aeroelastic module was introduced.

A single revolution was used to settle the structural response. The blade rotational velocity was then accelerated from 1400 to 1750 (rpm) over 5 revolutions. This acceleration mirrors the process conducted during the experiment. To determine the effect of the blade acceleration on its qualitative aeroelastic response, an additional simulation at the final rotational velocity value of 1750 (rpm) was conducted. Table 6 details the flow computational parameters.

Reynolds Number (-)	1.65×10^6
Starting Propeller Velocity (*rpm*)	1400
Final Propeller Velocity (*rpm*)	1750
Blade Pitch Angle ($^\circ$)$_{0.70R}$	27° 40′
Altitude (*m*)	*Sea-level*
Inflow Velocity (*m/s*)	0.0 (*Static conditions*)
Tip Velocity (*m/s*)	197.36
Tip Chord Length (*m*)	0.122
Turbulence Model	*URANS* $k-\omega$ *& SAS*

Table 6 Summary of the Commander propeller blade test conditions.

Structural Modelling

The blade was assumed to be of solid 1100 grade aluminum alloy, with a Young's Modulus of 6.9×10^{10} Pa, shear modulus of 2.6×10^{10} Pa and mass density of 2710 kg/m^3. The cross-sectional area, linear mass and blade inertia's are presented in Figure 4(a). The derived structural model includes the effects of the blade rotational force, with this varied to determine the Spoke diagram shown in Figure 4(b). The derived mode shapes match those seen within the experiment. For the aeroelastic simulations, the structural model focuses on, and uses, the first three modes. This was due to the fact that only the first three modes are reported as part of the experiment.

HMB3 has the ability to update the the active eigenmode through a blending feature. This is particularly useful when stiffening effects due to increasing rotational force are significant. However, looking at the Spoke diagram (Figure 4(b)), the stiffening effects are seen to be marginal for this blade. As a result, the modes shapes at the starting velocity of 1400 (rpm) are selected and kept constant throughout the simulation.

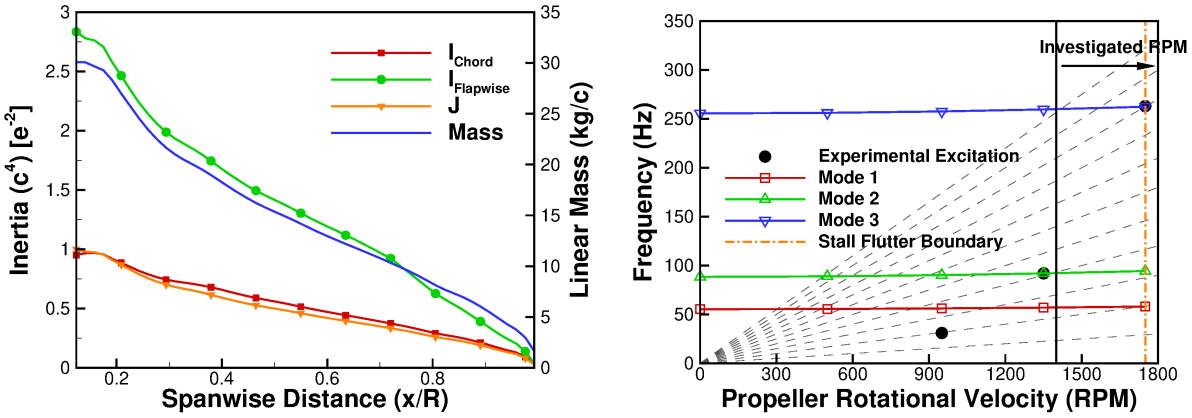

(a) Blade Structural Properties

(b) Blade Spoke Diagram

Fig. 4 Commander propeller blade structural properties and resultant frequencies.

Simulation Results

Dynamic stall investigation

Comparison of the quasi-3D results using SAS to standard 2D

Presented in Figure 5 are the aerodynamic loads for the NACA 0012 case, comparing 2D *URANS* and quasi-3D *SAS*, to experiments. In the experimental results, the pitching moment remains almost constant up until the aerofoil reaches its maximum angle. At this point, the negative pitching moment increases sharply due to the stalled flow. A similar response in found with the 2D *URANS* simulation, however, the peak pitching moment is found to be greater. The negative pitching moment for the quasi-3D *SAS* simulation is found to increase earlier, and this correlates with an increase in drag.

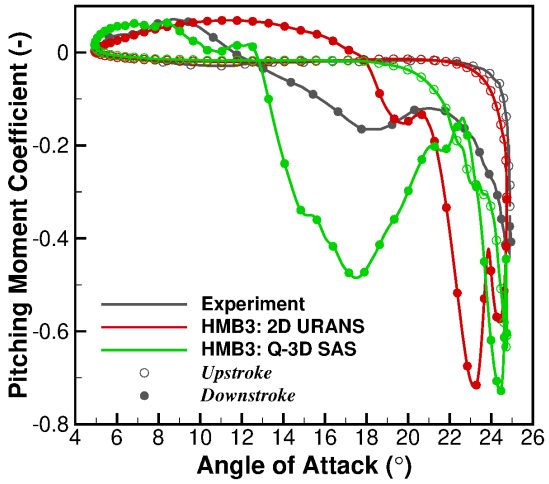

Fig. 5 Comparison of the NACA 0012 pitching moment coefficient for the 2D and quasi-3D simulations to the experimental results.

The recovery of the pitching moment during the experiment is found to occur over a range of 13°, eventually recovering and crossing the upstroke profile around 12°. During the downstroke, the 2D *URANS* is found to have a significant secondary stall event, resulting in two pitching moment peaks. The 2D *URANS* then quickly recovers, crossing the upstroke profile 6° earlier than experiments. This indicates that the 2D *URANS* simulation develops a closed stall bubble. This sheds from the section quickly, allowing the flow to attach sooner than seen during the experiment. For the quasi-3D *SAS*, following the peak, the pitching moment recovers to similar values as the experiment. The experimental pitching moment, during the downstroke, is seen to increase around 18°. This indicates the development of more separated flow between the 22 – 18° range. This is also present in the quasi-3D *SAS* simulation, however, the magnitude of this secondary event is found to be larger. The quasi-3D *SAS* simulation then begins to recover crossing the upstroke profile at the same angle as experiments.

Using the pitching moment curve, the aerodynamic damping of the system is estimated and presented in Table 7. Like in experiments, a negative damping value is seen for both 2D *URANS* and quasi-3D *SAS* simulations. However, due to the sharp recovery of the 2D *URANS* simulation, the positive anti-clockwise moment loop is greater than seen from the experiment, therefore the damping estimation is below the experiment. The quasi-3D *SAS* simulation provides a larger negative damping value for the phased average solution, at a closer percentage to the experiment than the 2D *URANS* . In addition, a scatter in the estimated aerodynamic damping of ±37% is observed for *SAS* due to cycle to cycle variations. So, the results are a better estimation of the experiments.

Table 7 NACA 0012 Aerodynamic Damping

Section	Modelling Method	Aerodynamic Damping
NACA 0012	Experiment	-0.350
	2D *URANS*	-0.204
	Quasi-3D *SAS*	-0.457

A transition was made to the Commander section calculations and the pitching moment results are presented in Figure 6. In terms of the *SAS* simulation, a significant effect can be seen on the stall behaviour and downstroke profile. Due to the shedding process captured via the *SAS* method, the pitching moment for the *SAS* simulation recovers shortly after the stall, thus producing the peak moment coefficient during the downstroke. This creates a negative moment loop which reduces the aerodynamic damping value, shown in Table 8.

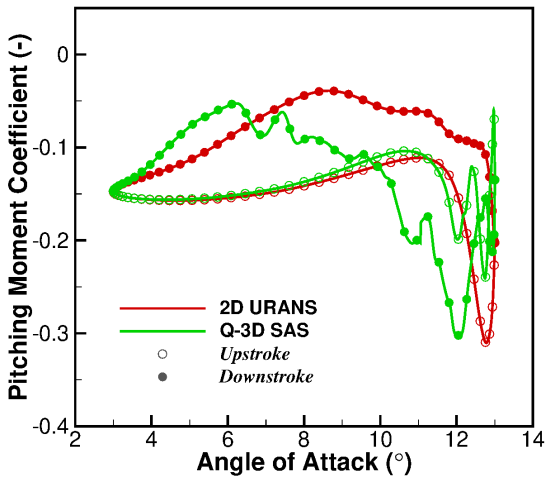

Fig. 6 Comparison of the pitching moment for the 90% *R* **Commander aerofoil section.**

Table 8 Commander 90% *R* Aerodynamic Damping

Section	Modelling Method	Aerodynamic Damping
90% *R*	2D *URANS*	0.491
	Quasi-3D *SAS*	0.104

Based upon this investigation, it is clear that the use of scale-resolving CFD methods, compared to *URANS*, has a significant effect on the dynamic stall predictions. For all tested aerofoils, the aerodynamic damping value is reduced as a result of the use of the *SAS* method. Overall and based upon the aerodynamic damping, the *SAS* method is shown to better capture the physics of a highly stalled dynamic test case, such as the NACA 0012 aerofoil investigated. In addition to this, these results suggest that stall flutter could be possible for the 90% *R* Commander station, but this has to be verified using 3D simulations.

Comparison between URANS and SAS for the 3D accelerating blade

Presented in Figure 7 is a comparison of the maximum relative torsional stress between the simulations and the experimental results. Both experiments and simulation results provide a simple quadratic response across the blade radius. The maximum stress value for the experiment is seen at the 75% *R* station. For both simulations, the maximum values are seen slightly outboard at 80% *R*. Comparing the relative values of the *URANS* and *SAS* simulations, the *SAS* simulation performs better with larger torsional stress values observed. Although the absolute values do not match exactly, the trend across the blade radius are very well captured. This indicates similar loading patterns are observed between the experiments and simulations.

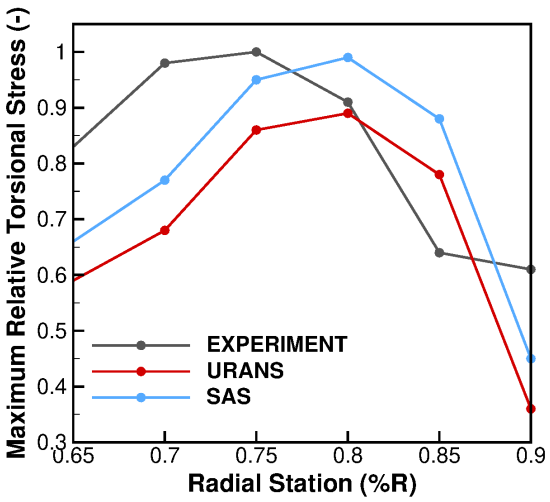

Fig. 7 Comparison of the maximum relative torsional stress, along the blade radius, between the experimental and simulation results.

In addition to the torsional stress levels, an analysis can be conducted on the structural response of the modal method. As the aeroelastic technique assumes the blade deflection is a combination of the supplied eigenmodes, modal amplitudes and forces are generated for each mode. Figure 8 presents the modal amplitudes for the three modes supplied. Looking at the first mode (chord-wise bending mode) an oscillating response of 2.54 $/revolution$ around a linearly increasing mean value is observed for the *URANS* simulation. A similar response is found for the *SAS*, with a frequency of 2.46 $/revolution$, however, the periodic amplitude increases for the *SAS* computation by 20% during the transition phase. This increases to a factor of 3 by the final revolutions.

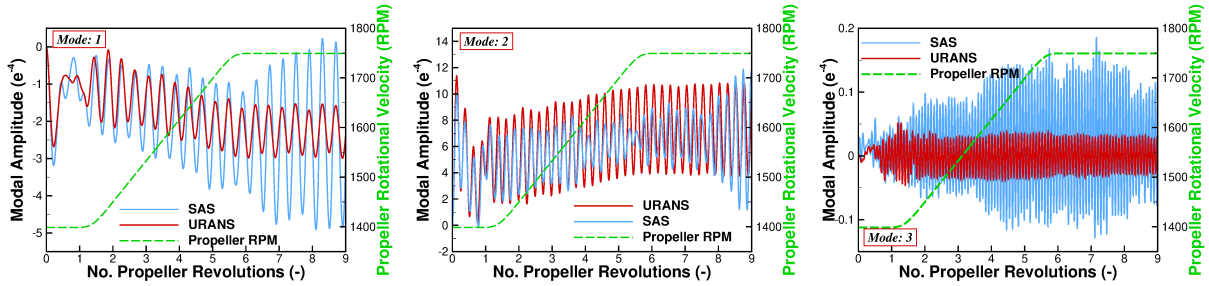

(a) Mode 1. (b) Mode 2. (c) Mode 3.

Fig. 8 Modal amplitude response for the Commander blade.

During the transition phase for the second mode, a decrease in periodic amplitude is found for the *SAS* simulation. This is a result of the current mode being of flap-wise bending type. As previously described within Section III the modal amplitudes are calculated based upon the modal forces and these modal forces are a projection of the nodal point pressure onto the interpolated mode shape. Therefore, a decrease in modal amplitude indicates a decrease in modal force, and as a result a potential increase in detached flow due to the use of *SAS* . Once the *SAS* simulation reaches the final rotational velocity, the periodic amplitude gradually increases to 66% of the transition value.

During the experiments of DOWTY, it was found that the first torsional mode was triggered. From Figure 8(c) a significant difference is found between the *URANS* and *SAS* response. For the *URANS* simulation, the modal amplitude oscillates at a frequency of 11.3 $/revolution$ around a constant mean value with a constant periodic amplitude. For the *SAS* computation, the periodic amplitude grows during the transition phase, with a significant step change seen during the 4^{th} propeller revolution. During this step change the periodic amplitude increases by a factor of 2. The rotational velocity at this point is 1600 (rpm), and this correlates to the step change in torsional stress seen during the experiment. Once the acceleration is complete, the periodic amplitude continues to increase to 3 times the original transition value.

For the frequency response of the modal amplitude, a Fast-Fourier-Transform was conducted on each signal, and this is presented in Figure 9 for the *URANS* and *SAS* simulations. As can be seen for both computations, non-integer harmonics are present for all modes. This gives an indication of the presence of stall on the blade. Larger amplitudes are observed for the *SAS* simulation with additional noise also appearing around the main frequency peaks. The obtained

frequencies for the three modes relate to the observed natural frequencies seen in the Spoke diagram in Figure 4(b). From the Spoke diagram: Mode 1 is observed to have a response between 2^{nd} and 3^{rd} order; Mode 2 has a 4^{th} order response; and Mode 3 is found to have a 11^{th} order response. This is what is seen from the FFT of the modal amplitudes.

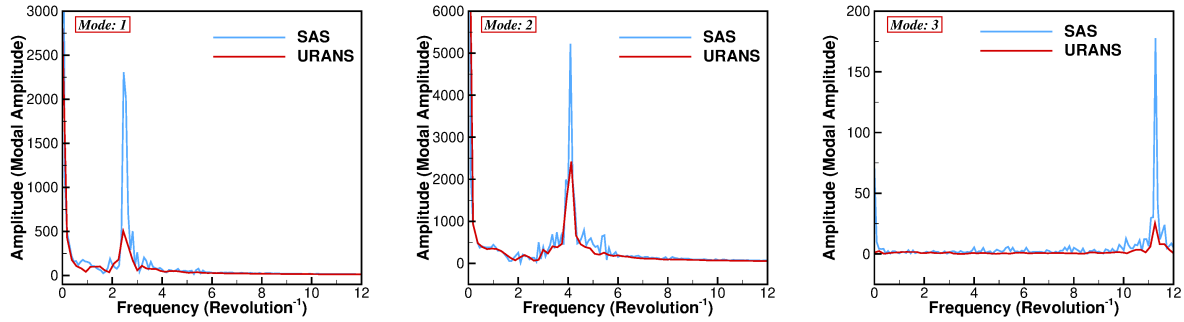

(a) Mode 1. (b) Mode 2. (c) Mode 3.

Fig. 9 FFT of the modal amplitude response for the Commander blade.

Presented in Figure 10 is the flow visualisation of the non-dimensional tangential velocity for the *URANS* and *SAS* simulation using radial slices at 90%R for the maximum torsional stress time-step. For the *URANS* simulation, a stable velocity profile is observed. Recirculating flow is present along the observed region, but remains fixed to the blade surface. The *SAS* results provide much greater variations in unsteady content compared to the *URANS*. As can be seen from Figure 10(b), an open stall bubble is produced with several vortex structures present. This open bubble indicates the flow is being shed from the blade surface, providing a negative aerodynamic damping response to the structure.

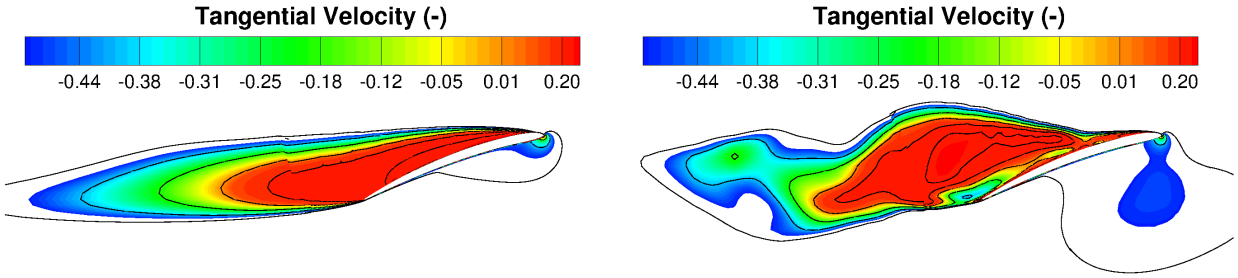

(a) *URANS* : 90% R (b) *SAS* : 90% R

Fig. 10 Flow visualisation of the non-dimensional tangential velocity using radial slices for the accelerating blade simulations.

In terms of the entire flow-field a visualisation of the vorticity magnitude iso-surfaces of value 1.0 is presented in Figure 11 for the *URANS* and *SAS* simulations. Looking at the *URANS* solution and focusing at the maximum torsional stress time-step, the detached flow bubble present towards the tip of the blade is clearly present. This projects inboard until the 70% station. Towards the blade root, a detached flow bubble present towards the trailing edge. During the blade acceleration, the inboard detached flow begins to project along the blade and interact with the tip bubble creating an additional bubble around mid span.

For the *SAS* simulation, from the 30% to 70% station the flow has detached at the trailing edge. Unlike the *URANS* iso-surfaces, greater fluctuation in the *SAS* iso-surfaces are found. As the blade is accelerated, the iso-surfaces shed at an increasing rate. This results in increased fluctuations of the surface loads causing variations in the periodic amplitude of the *SAS* modal response.

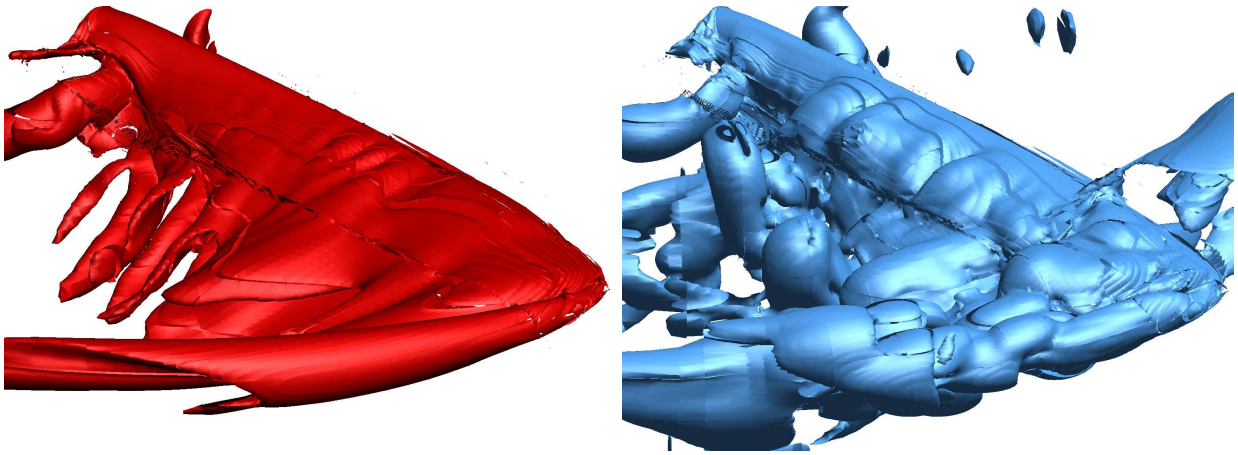

(a) *URANS* (b) *SAS*

Fig. 11 Flow visualisation using vorticity magnitude iso-surface of $|\omega| = 1.0$.

Presented in Figure 12 are the surface pressure coefficients contours along the upper surface of the blade, at the maximum torsional stress time-step, for the *URANS* and *SAS* simulations. Focusing on the *URANS* simulation results (Figure 12(a)), two clear stations indicate the presence of stall. Flat pressure contours are observed at the blade tip and mid-span. The tip stall is present throughout the simulation and only grows in size as the blade is accelerated. The mid-span stall develops during the transition phase, with the presence of this stall bubble visible from the *URANS* iso-surfaces (Figure 11(a)).

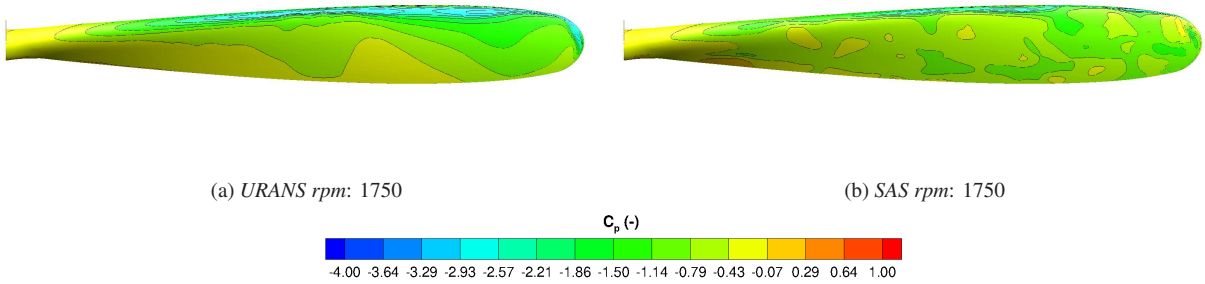

(a) *URANS rpm*: 1750 (b) *SAS rpm*: 1750

Fig. 12 Visualisation of the surface pressure coefficients for the *URANS* and *SAS* simulations.

For the *SAS* simulation result (Figure 12(b)), a significant variation in the pressure profile is observed. As the blade is time-marched, detached flow from the root begins to project towards the tip, interacting with the stalled flow present outboard. Similarities can be drawn between the *URANS* and *SAS* simulations; towards the tip of the blade an almost constant pressure contour is observed, with an increase in the amount of lower pressure seen during the acceleration. Pockets of high pressure are also observed during the acceleration. This is a result of the attempted reattachment of the flow to that section, as the vortex is shed from the blade.

To determine the overall fluctuation in surface pressure, a Fast-Fourier Transform was conducted on selected block faces of the propeller upper surface. This is shown in Figure 13 for the *URANS* and *SAS* simulations. As can be seen, a larger amount of frequency content is captured via the *SAS* simulation, with almost no significant peaks captured using *URANS* .

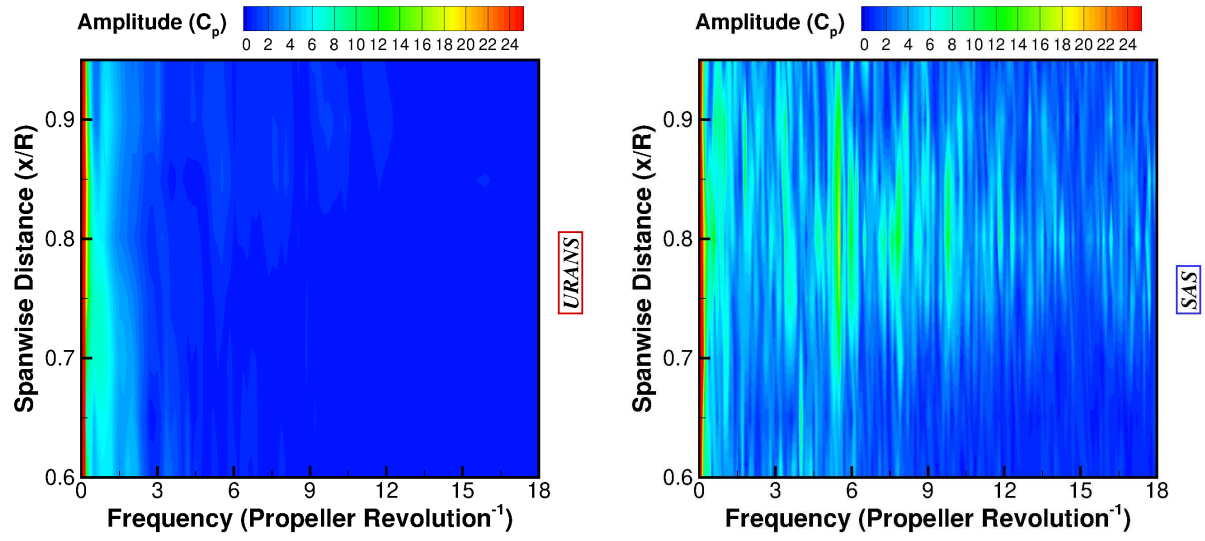

(a) *URANS* (b) *SAS*

Fig. 13 FFT of the surface pressure coefficient along the upper surface of the blade.

Investigating the effect of the blade acceleration

To determine the effect of the blade acceleration, a simulation at a fixed rotational velocity of 1750 (rpm) using the *SAS* model was conducted. For this simulation, the mode shapes and frequencies were updated to correlate with the current rotational velocity. A rigid solution at 1750 (rpm) was produced from which to start this calculation.

In a similar manner to the accelerating blade simulation, a comparison of the maximum relative torsional stress can be seen in Figure 14. For the fixed rpm simulation, a linear trend in the torsional stress is observed across the blade. This varies significantly from the experimental and accelerating blade simulations where a quadratic response is seen. The change in response is a result of greater fluctuation in modal force seen for the fixed rpm modes during the aeroelastic start up. As previously described, high levels of structural damping are used to control the initial oscillation of the aeroelastic blade. This level of damping is kept constant, combine this with the fact greater levels of force are seen during the initial revolutions of the fixed rpm simulation compared to the accelerating blade, greater oscillations are observed impacting the final deformation results. Based upon this and in order to capture the same physics as the experiment, it is observed that the acceleration of the blade is critical.

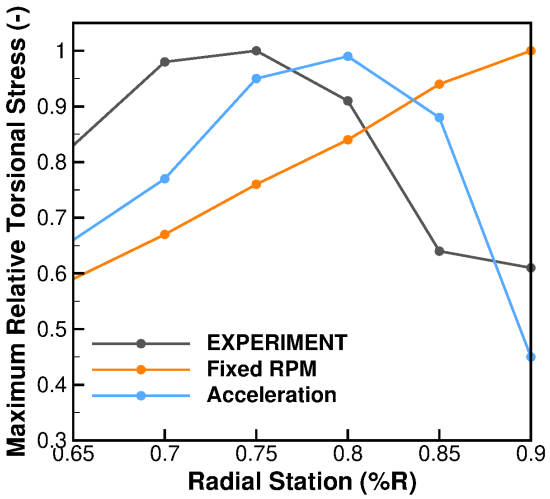

Fig. 14 Comparison of the maximum relative torsional stress, along the blade radius, between the accelerating and fixed *rpm* simulations.

Presented in Figure 15 is the comparison of the modal amplitude between the fixed rpm and accelerating blade simulations. For the accelerating blade, the comparison is focused on the last revolution of the acceleration and the five revolutions at the final state. Focusing on Mode 1 and for the fixed rpm simulation, there is a slight increase in mean value of 15%. The response of both simulations, however, remain similar. The frequency response of Mode 1 is presented in Figure 16(a). A reduction of 0.6 $/revolution$ in frequency for the fixed simulation is found, with a reduction in periodic amplitude of 12%.

For Mode 2, the periodic amplitude of the fixed rpm simulation is found to be 130% greater than the accelerating blade during the initial two revolutions. As the accelerating blade modal amplitude begins to diverge, this difference is reversed with the fixed rpm simulation periodic amplitude found to be 23% smaller than the accelerating blade during the final two revolutions of comparison. Overall, there is an 8% reduction in periodic amplitude for the fixed rpm simulation, with a 20% reduction in the frequency response, as is shown in Figure 16(b).

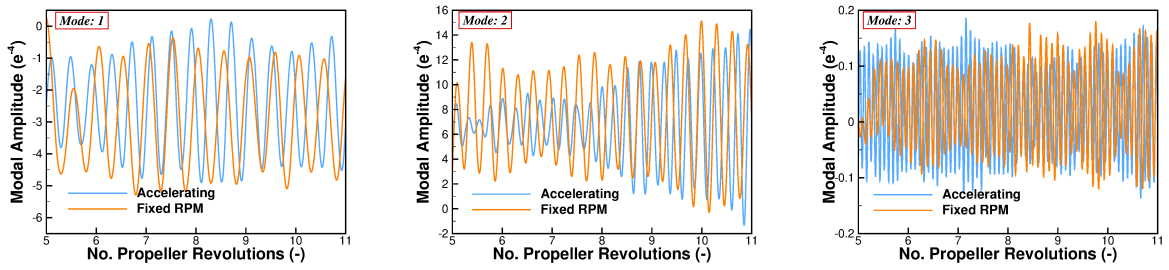

(a) Mode 1. (b) Mode 2. (c) Mode 3.

Fig. 15 Comparison of the modal amplitude response between the accelerating blade and fixed *RPM* simulations.

For the final mode, similar profiles are observed between the accelerating blade and fixed rpm simulations. Due to the instability of this mode, the difference in periodic amplitude fluctuates between the simulations. For the initial two revolutions of comparison, the accelerating blade simulation is seen to have a periodic amplitude 20% greater than the fixed rpm. This reverses during revolutions 8 to 10, where the fixed rpm simulation is seen to have a periodic amplitude 73% greater than the accelerating blade. Overall, a 20% reduction in periodic amplitude is observed for the fixed rpm simulation with a reduction in frequency of 20%.

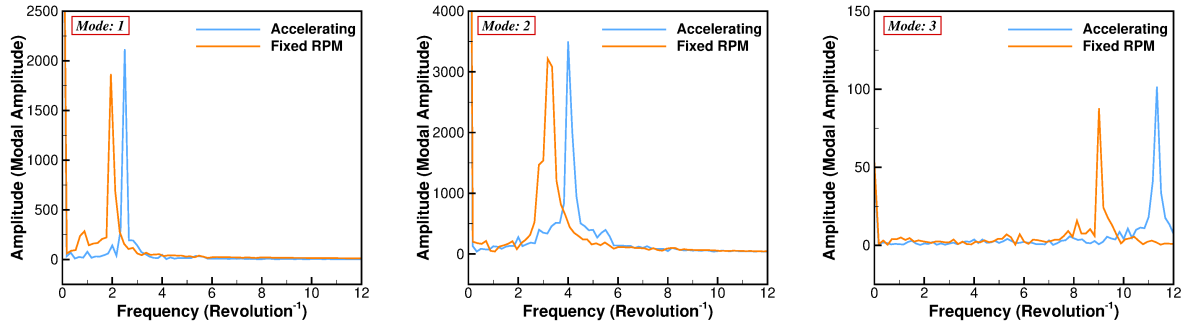

(a) Mode 1. (b) Mode 2. (c) Mode 3.

Fig. 16 A comparison of the modal amplitude frequency response for the accelerating and fixed *RPM* simulations.

To summarise, regardless of ramping or fixed rpm, all *SAS* simulations show blade excitation and this agrees qualitatively with the tests. However, in order to capture the physics seen during the experiments, the acceleration of the blade is required.

Conclusions

A successful time-marching aeroelastic method using CFD has been derived, with the quality of the computational mesh preserved throughout the calculation. For the Commander propeller blade, qualitative agreement can be found between the simulation results and experiments, whilst using the *SAS* simulation model for the accelerating blade. An absolute correlation between the torsional stress levels was not seen, however the trend of stress across the blade radius are predicted well for the *SAS* simulation. A qualitative comparison of the modal amplitude response is presented with an unstable solution was achieved for the *SAS* computation. The *URANS* calculation did not provide such a response, and therefore, this highlights the need for scale-resolving CFD methods for stall flutter predictions.

A comparison was also made between the accelerating blade and fixed rpm simulations. In terms of the modal response, similar profiles are observed between the simulations with a reduction in frequency seen for all modes. However, the response seen in terms of the torsional stress distribution across the blade radius for the fixed rpm simulation did not correlate to the experiment. As a result, to mirror the response seen in the experiment, the acceleration of the blade is seen as critical to the evaluation of torsional stress.

This investigation was found to be limited in terms of experimentally measured parameters and test cases. As a result, there is a clear need for modern data for stall flutter, from test designs with method validation its objective.

Acknowledgments

The support provided by DOWTY Propellers is gratefully acknowledged.

References

[1] Sterne, L., "Spinning Tests on Fluttering Propellers," *Aeronautical Research Council: Reports and Memoranda*, , No. 2022, 1945.

[2] Baker, J., "The effects of various parameters, including Mach number, on propeller-blade flutter with emphasis on stall flutter," Tech. Rep. 3357, National Advisory Commitee for Aeronautics, 1955.

[3] Hubbard, H., Burges, M., and Sylvester, M., "Flutter of thin propeller blades, including effects of Mach number, structural damping, and vibratory-stress measurements near the flutter boundaries," Tech. Rep. 3707, National Advisory Commitee for Aeronautics, 1956.

[4] Burton, P., "Straingauge Test Report on a Spin Test Carried out on a Type (c) R.305/3-82-F/6 Propeller on the Spinning Tower at the R.A.E. Farnborough, Hants." Tech. Rep. 093.1.592, DOWTY ROTOL LTD., 1979.

[5] Smith, A., "Analysis and Test Evaluation fo the Dynamic Stability of Three Advanced Turboprop Models at Zero Forward Speeds," Contractor Report 175025, National Aeronautics and Space Administration, 1985.

[6] Reddy, T., and Kaza, K., "Analysis of an Unswept Propfan Blade with a Semiempirical Dynamic Stall Model," Technical Memorandum, National Aeronautics and Space Administration, 1989.

[7] Gormont, R., "A Mathematical Modal of Unsteady Aerodynamics and Radial Flow for Application to Helicopter Rotors," Tech. Rep. AD-767 240, US Army Air Mobility Research and Development Laboratory, 1973.

[8] Delamore-Sutcliffe, D., "Modelling of Unsteady Stall Aerodynamics and Prediction of Stall Flutter Boundaries for Wings and Propellers," Ph.D. thesis, University of Bristol, 2007.

[9] Ognev, V., and Rosen, A., "Influence of using various unsteady aerodynamic models on propeller flutter prediction," *Journal of Aircraft*, Vol. 48, No. 5, 2011.

[10] Verstraelen, E., Habib, G., Kerschen, G., and Dimitriadis, G., "Experimental Passive Flutter Suppression Using a Linear Tuned Vibration Absorber," *AIAA Journal*, Vol. 55, No. 4, 2017. DOI: 10.2514/1.J055397.

[11] Razak, N., Andrianne, T., and Dimitriadis, G., "Flutter and Stall Flutter of a Rectangular Wing in a Wind Tunnel," *AIAA Journal*, Vol. 49, No. 10, 2011. DOI: 10.2514/1.J051041.

[12] Yamasaki, M., Isogai, K., Uchida, T., and Yukimura, I., "Shock-Stall Flutter of a Two-Dimensional Airfoil," *AIAA Journal*, Vol. 42, No. 2, 2004. DOI: 10.2514/1.9088.

[13] Culler, E., and Farnsowrth, J., "Higher frequencies in stall flutter moment development," *Journal of Fluids and Structures*, Vol. 85, 2019. DOI: 10.1016/j.jfluidstructs.2019.01.007.

[14] Culler, E., Fagley, C., Seidel, J., McLaughlin, T., and Farnsworth, J., "Developing a reduced order model from structural kinematic measurements of a flexible finite span wing in stall flutter," *Journal of Fluids and Structures*, Vol. 71, 2017. DOI: 10.1016/j.jfluidstructs.2017.03.010.

[15] Bryant, M., Gomez, J., and Garcia, E., "Reduced-Order aerodynamic modeling of flapping wing energy harvesting at low reynolds number," *AIAA Journal*, Vol. 51, No. 12, 2013. DOI: 10.2514/1.J052364.

[16] Arena, A., Lacarbonara, W., and Marzocca, P., "Nonlinear Aeroelastic Formulation and Postflutter Analysis of Flexible High-Aspect-Ratio Wings," *Journal or Aircaft*, Vol. 50, No. 6, 2013. DOI: 10.2514/1.C032145.

[17] Dehaeze, F., and Barakos, G., "Mesh deformation method for rotor flows," *Journal of Aircraft*, Vol. 49, No. 1, 2012, pp. 82–92.

[18] Chirico, G., Barakos, G., and Bown, N., "Numerical aeroacoustic analysis of propeller designs," *The Aeronautical Journal*, Vol. 122, No. 1248, 2018, pp. 283–315. DOI: 10.1017/aer.2017.123.

[19] Crozon, C., Steijl, R., and Barakos, G., "Coupled flight dynamics and CFD - demonstration for helicopters in shipborne environment," *The Aeronautical Journal*, Vol. 122, No. 1247, 2018, pp. 42–82.

[20] Babu, S., Loupy, G., Dehaeze, F., Barakos, G., and Taylor, N., "Aeroelastic simulations of stores in weapon bays using Detached-Eddy Simulation," *Journal of Fluids and Structures*, Vol. 66, 2016, pp. 207–228. Doi:10.1016/j.jfluidstructs.2016.07.014.

[21] Scrase, N., and Maina, M., "The Evaluation of Propeller Aero-acoustic Design Methods by Means of Scaled-Model Testing Employing Pressure Tapped Blades and Spinner," *19th ICAS Congress*, 1994.

[22] Gomariz-Sancha, A., Maina, M., and Peace, A., "Analysis of propeller-airframe interaction effects through a combined numerical simulation and wind-tunnel testing approach," *AIAA SciTech Forum, 53rd AIAA Aerospace Sciences Meeting*, AIAA, Kissimmee, Florida, 2015, pp. 1–19.

[23] Knepper, A., and Bown, N., "IMPACTA Wind-tunnel Instrumentation Specification," Tech. Rep. ITS 01777, Issue 3, Dowty Propellers (GE Aviation Systems Ltd), 2014.

[24] Barakos, G., and Johnson, C., "Acoustic comparison of propellers," *International Journal of Aeroacoustics*, Vol. 15, No. 6-7, 2016, pp. 575–594. DOI: 10.1177/1475472X16659214.

[25] Barakos, G., Steijl, R., Badcock, K., and Brocklehurst, A., "Development of CFD capability for full helicopter engineering analysis," *31st European Rotorcraft Forum, Florence, Italy*, 2005.

[26] Steijl, R., Barakos, G., and Badcock, K., "A framework for CFD analysis of helicopter rotors in hover and forward flight," *International Journal of Numerical Methods in Fluids*, Vol. 51, No. 8, 2006. DOI: 10.1002/fld.1086.

[27] Lawson, S., Woodgate, W., Steijl, R., and Barakos, G., "High performance computing for challenging problems in computational fluid dynamics," *Progress in Aerospace Sciences*, Vol. 52, 2012. DOI: 10.1016/j.paerosci.2012.03.004.

[28] Menter, F., and Egorov, Y., "The Scale-Adaptive Simulation Method for Unsteady Turbulent Flow Predictions. Part 1: Theory and Model Description," *Flow, Turbulence and Combustion*, Vol. 85, No. 1, 2010.

[29] Menter, F., and Egorov, Y., "A Scale Adaptive Simulation Model using Two-Equation Models." *43rd AIAA Aerospace Sciences Meeting and Exhibit*, 2005.

[30] Babu, S., Zografakis, G., Barakos, G., and Kusyumov, A., "Evaluation of scale-adaptive simulation for transonic cavity flows," *International Journal of Engineering Systems Modelling and Simulation*, Vol. 8, No. 2, 2016. DOI: 10.1504/IJESMS.2016.075510.

[31] Loupy, G., Barakos, G., and Taylor, N., "Multi-disciplinary simulations of stores in weapon bays using scale adaptive simulation," *Journal of Fluids and Structures*, Vol. 81, 2018. DOI: 10.1016/j.jfluidstructs.2018.05.012.

[32] Jarkowski, M., Woodgate, M., Barakos, G., and Rokicki, J., "Towards Consistent Hybrid Overset Mesh Methods for Rotorcraft CFD," *International Journal for Numerical Methods in Fluids*, Vol. 74, No. 8, 2014, pp. 543–576. Doi:10.1002/fld.3861.

[33] Shepard, D., "A Two-dimensional Interpolation Function for Irregularly-spaced Data," *Proceedings of the 1968 23rd ACM National Conference*, New York, NY, USA, 1968.

[34] Biava, M., and Barakos, G., "Optimisation of Ducted Propellers for Hybrid Air Vehicles Using High-Fidelity CFD," *The Aeronautical Journal*, Vol. 120, No. 1232, 2016, pp. 1632–1657. Doi:10.1017/aer.2016.78.

[35] Renka, R., "Multivariate Interpolation of Large Sets of Scattered Data," *ACM Trans. Math. Softw.*, 1988, pp. 139 – 148. Doi:10.1145/45054.45055.

[36] Bonet, J., and Peraire, J., "An alternating digital tree (ADT) algorithm for 3D geometric searching and intersection problems," *International Journal for Numerical Methods in Engineering*, Vol. 31, No. 1, 1991, pp. 1–17. Doi:10.1002/nme.1620310102.

[37] Corke, T., and Thomas, F., "Dynamic Stall in Pitching Airfoils: Aerodynamic Damping and Compressibility Effects," *Annual Review of Fluid Mechanics*, Vol. 47, 2015.

[38] McAlister, K., Pucci, S., McCroskey, W., and Carr, L., "An Experimental Study of Dynamic Stall on Advanced Airfoil Sections Volume 2: Pressure and orce Data," Tech. Rep. TM-84245, National Aeronautics and Space Administration, 1982.